Available online at www.sciencedirect.com

ScienceDirect

Advances in Space Research xxx (xxxx) xxx

ADVANCES IN SPACE RESEARCH (a COSPAR publication)

www.elsevier.com/locate/asr

Relative and absolute on-board optimal formation acquisition and keeping for scientific activities in high-drag low-orbit environment

Enrico Belloni *, Stefano Silvestrini, Jacopo Prinetto, Michèle Lavagna

Politecnico di Milano, Via La Masa 34, 20156 Milano, Italy

Received 11 November 2022; received in revised form 20 July 2023; accepted 23 July 2023

Abstract

In this paper, a novel Model Predictive Control (MPC) technique for multi-satellite formation flying geometry acquisition and maintenance in high-drag environment is presented. The proposed MPC relies on a linearized and convexified quasi-nonsingular Relative Orbital Elements (ROE) model based on state transition matrices propagation, allowing to include the effect of perturbations in the prediction to optimize fuel efficiency and tracking accuracy. The formation is controlled with respect to a non-decaying orbiting point to perform absolute and relative station keeping simultaneously. For this purpose, a new dedicated plant matrix to include drag effects on ROE in the propagation is derived and validated with respect to numerical results. In all simulations, the satellites are assumed to be equipped with a single low-thrust propulsion unit, therefore, specific constraints are included in the controller to obtain a feasible solution in a real operational scenario. Moreover, a collision avoidance constraint is added in case of close proximity operations exploiting a linear mapping between the set of ROE and cartesian coordinates expressed in the Local-Vertical-Local-Horizontal (LVLH) reference frame. The controller response is simulated in several realistic mission contexts with a high-fidelity orbital propagator and the results are validated for fuel efficiency by comparing them to similar approaches available in literature and to optimal solutions obtained respectively with a direct single shooting algorithm and with a closed-form impulsive formulation.

Keywords: Relative orbital elements; Model-predictive control; Formation flying; Convex optimization; Drag compensation

1. Introduction

In the last few decades, the attention on multi-satellite missions grew constantly over the years. The traditional approach to space has always been to build a big monolithic satellite that would deal with all the tasks. However, the development of new technologies allows to split the duties of a single spacecraft between multiple smaller units flying in formation, with several advantages in terms of reliability and scientific return. Distributed systems in particular provide the highest degree of robustness, being constituted by independent satellites which are capable of exchanging information and computing the command and trajectory of the entire formation. The main challenge thus is to design robust guidance, navigation, and control (GNC) techniques for spaceborne distributed systems that are viable for onboard implementation, as autonomy is mandatory in presence of close spacecraft separations or limited communication windows with ground control.

Several solutions have been provided in recent years literature on the topic, each proving its advantages and disadvantages. A first solution is impulsive control, for which even closed-form solutions exist (Chernick and D'Amico, 2018), but these cannot be applied for low-thrust applications. A suitable option for continuous

* Corresponding author.
E-mail addresses: enrico.belloni@polimi.it (E. Belloni), stefano.silvestrini@polimi.it (S. Silvestrini), jacopo.prinetto@polimi.it (J. Prinetto), michelle.lavagna@polimi.it (M. Lavagna).

https://doi.org/10.1016/j.asr.2023.07.051
0273-1177/

low-thrust control is to use a Linear Quadratic Regulator (LQR) built on the linearized dynamics. However, even if this is an optimal technique, it is hard to include constraints on the solution, which therefore may result to be unfeasible when real operational constraints are present, since this technique often implies continuous firing. Similar limitations exist for nonlinear control with Lyapunov functions. A different option is the use of Artificial Potential Fields (APF) as a guidance layer to generate the trajectory to follow by a chaser spacecraft, originally developed as spring-like functions (McInnes, 1995; Palmerini, 1999) and then reformulated for applications more similar to this paper case-study in recent approaches (Steindorf et al., 2017; Silvestrini et al., 2019; Silvestrini and Lavagna, 2021). This method allows an easy and natural implementation of collision avoidance constraints, but may often lead to instabilities and lacks a measure of optimality. Direct and indirect optimization techniques can find optimal solutions (Wu et al., 2009), and have been recently applied with relative motion formulations based on Jordan normal form (Bai et al., 2021; Bai et al., 2023), however these methods may be inadequate in highly perturbed unpredictable environment, where the capability for the spacecraft to react autonomously is crucial. The use of Jordan form for relative dynamics was also successfully tested by Zheng et al. (2019) in a Hamiltonian structure-preserving (HSP) controller in combination with APF. A technique that ensures the sub-optimality of the solution while allowing easy implementation of constraints is Model Predictive Control (MPC). The main drawback of MPC is the computational burden imposed on the hardware that, however, can be relaxed without loss of accuracy with a correct convexification of the problem.

The formulation of a convexified guidance and control problem for formation reconfiguration has been studied in several instances. Acikmese et al. (2012) proposed a fuel-optimal open-loop convex guidance algorithm for formation reconfiguration suitable for on-board implementation including collision avoidance. Morgan et al. (2014) proposed both an optimal guidance solution and a Model Predictive Control implementation for reconfiguration of spacecraft swarms between J2 invariant orbits, again including collision avoidance. Sarno et al. (2020) proposed a similar method for autonomous formation reconfiguration of distributed systems, adding a task-assignment strategy optimizing via a genetic algorithm. Finally, Scala et al. (2021) proposed a design strategy of optimal low-thrust maneuvers for remote sensing multi-satellite formations flying in LEO. In all the listed references the state of the satellites is expressed in the chief-centered local Local-Vertical-Local-Horizontal (LVLH) reference frame represented in Fig. 1.

Starting from previous work, this paper aims at enlarging the available literature on the topic by providing a solution that couples relative and absolute orbit control in high-drag environments while directly employing a state expressed in Relative Orbital Elements (ROE). In particular, a novel Model Predictive Control (MPC) acting on a single low-thrust propulsion unit is introduced. The MPC exploits a linear propagation of the dynamics in Relative Orbital Elements, allowing the inclusion of J2 effect and drag in the optimization problem while keeping the computational effort reduced. The formation is controlled with respect to a non-decaying orbiting point in order to perform absolute and relative station keeping simultaneously. For this purpose, a dedicated plant matrix to include drag effects in the propagation is derived and validated with respect to numerical results. The problem is also convexified to allow the use of fast optimization tools viable for autonomous control and on-board implementation. Constraints are introduced to simulate the presence of a single engine on board by providing limits of thrust module, thrusting angles, and slew rates, in order to obtain feasible control profiles for an average micro-satellite. In addition, a collision avoidance constraint is included to ensure safety in presence of proximity operations.

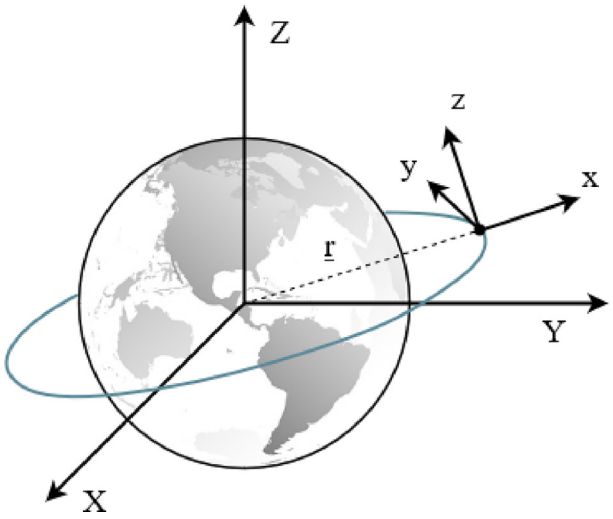

Fig. 1. Local-Vertical-Local-Horizontal reference frame representation with respect to the Earth-Centered Inertial (ECI) reference frame. X axis coincides with Vernal equinox.

2. Dynamics model

As anticipated previously, the relative motion between the satellites is modeled by expressing the state of the satellites in terms of the quasi-nonsingular Relative Orbital Elements introduced by D'Amico (2010) in his PhD thesis. These are nonlinear combinations of mean orbital elements (MOE), shown in Eq. (1), which allow to easily introduce the effect of perturbations by linearly propagating the system with plant matrices. ROE representations are better connected to the physics and relative motion geometry, in addition, they are valid in non-circular orbits and for large spacecraft separations, showing several advantages with respect to the commonly used Hills-Clohessy-Wiltshire (HCW) equations (Clohessy and Wiltshire, 1960), which imply a representation in the chief-centered LVLH

reference frame. Moreover, their slowly varying nature is beneficial to computational efficiency.

$$\begin{pmatrix} \delta a \\ \delta\lambda \\ \delta e_x \\ \delta e_y \\ \delta i_x \\ \delta i_y \end{pmatrix} = \begin{pmatrix} (a-a_c)/a_c \\ u-u_c+(\Omega-\Omega_c)\cdot\cos(i_c) \\ e\cdot\cos(\omega)-e_c\cdot\cos(\omega_c) \\ e\cdot\sin(\omega)-e_c\cdot\sin(\omega_c) \\ i-i_c \\ (\Omega-\Omega_c)\cdot\sin(i_c) \end{pmatrix} \tag{1}$$

In the previous set of equalities, $u=\omega+M$ is the mean argument of latitude and the subscript c refers to the chief satellite with respect to which the relative dynamics of each deputy spacecraft and the local LVLH reference system are defined.

In general, perturbations causing a variation of orbital elements are of two types, conservative and non-conservative. In the second instance, as in presence of differential drag, the perturbing effect depends not only on the differences in the orbit geometry, but also on the difference between satellite features, represented by a ballistic coefficient difference ΔB in this case. This parameter is therefore included as the last term in an augmented state representation, which will be used for the propagation of the dynamics.

$$\boldsymbol{\delta\underline{\alpha}} = \begin{pmatrix} \delta a \\ \delta\lambda \\ \delta e_x \\ \delta e_y \\ \delta i_x \\ \delta i_y \\ \Delta B \end{pmatrix} = \begin{pmatrix} (a-a_c)/a_c \\ u-u_c+(\Omega-\Omega_c)\cdot\cos(i_c) \\ e\cdot\cos(\omega)-e_c\cdot\cos(\omega_c) \\ e\cdot\sin(\omega)-e_c\cdot\sin(\omega_c) \\ i-i_c \\ (\Omega-\Omega_c)\cdot\sin(i_c) \\ (B-B_c)/B \end{pmatrix} \tag{2}$$

The natural ROE dynamics of the system is linearly propagated by defining a plant matrix $\mathbf{A}$, obtained as the sum of the plant matrices relative to keplerian motion and all considered perturbations. Since the following study will be focused on formations flying in Low Earth Orbit (LEO), only J2 and atmospheric drag will be included:

$$\mathbf{A} = \mathbf{A_{kep}} + \mathbf{A_{J2}} + \mathbf{A_{drag}} \tag{3}$$

Adding the control term, the linearized dynamics for the j-th satellite of the formation can be expressed in the form:

$$\dot{\underline{\mathbf{x}}}_\mathbf{j}(t) = \mathbf{A}(t)\underline{\mathbf{x}}_\mathbf{j}(t) + \mathbf{B}(t)\underline{\mathbf{u}}_\mathbf{j}(t) \tag{4}$$

where $\underline{\mathbf{x}} = \boldsymbol{\delta\underline{\alpha}} = \left(\delta a, \delta\lambda, \delta e_x, \delta e_y, \delta i_x, \delta i_y, \Delta B\right)^T$ is the augmented vector of quasi-nonsingular Relative Orbital Elements, $\mathbf{A}$ is the plant matrix describing the natural evolution of the system including orbital perturbations, $\mathbf{B}$ is the control matrix, and $\underline{\mathbf{u}}$ is the control input in LVLH coordinates.

2.1. Keplerian motion

In the Keplerian two-body problem, the general linearized relative motion of a deputy satellite relative to the chief for arbitrary eccentricities is described in terms of ROE as reported by Guffanti et al. (2017):

$$\delta\lambda(t) = -\frac{3}{2}n_c(t-t_0)\delta a_0 + \delta\lambda_0 \tag{5}$$

where n_c is the chief mean motion, and the "0" subscript indicates quantities at initial time. From the previous expression, a simple plant matrix $\mathbf{A_{kep}}$ can be retrieved as:

$$\mathbf{A_{kep}} = \begin{bmatrix} 0 & 0 & 0 & 0 & 0 & 0 & 0 \\ -\frac{3}{2}n_c & 0 & 0 & 0 & 0 & 0 & 0 \\ 0 & 0 & 0 & 0 & 0 & 0 & 0 \\ 0 & 0 & 0 & 0 & 0 & 0 & 0 \\ 0 & 0 & 0 & 0 & 0 & 0 & 0 \\ 0 & 0 & 0 & 0 & 0 & 0 & 0 \\ 0 & 0 & 0 & 0 & 0 & 0 & 0 \end{bmatrix} \tag{6}$$

It is evident that keplerian relative motion depends only on the relative semi-major axis difference. Accordingly, the only nonzero higher-order terms will be proportional to powers of δa. Therefore, this plant matrix is valid for unperturbed orbits with small δa and arbitrary separation in all other state components (Koenig et al., 2017).

2.2. J2 effect

The J2 plant matrix can be retrieved from the differential effect of the earth oblateness acting on the chief and on the deputy. In particular, first-order secular effects of the second-order zonal geopotential harmonic J2 on the orbit geometry are included in the ROE propagation. The formulation that will be used is the one introduced by Guffanti et al. (2017) and reported in the following:

$$\mathbf{A_{J2}} = \kappa_{J2}\cdot\begin{bmatrix} 0 & 0 & 0 & 0 & 0 & 0 & 0 \\ -\frac{7}{2}EP & 0 & e_xGFP & e_yGFP & -FS & 0 & 0 \\ \frac{7}{2}e_yQ & 0 & -4e_xe_yGQ & -\left(1+4Ge_y^2\right)Q & 5e_yS & 0 & 0 \\ -\frac{7}{2}e_yQ & 0 & \left(1+4Ge_x^2\right)Q & 4e_xe_yGQ & -5e_xS & 0 & 0 \\ 0 & 0 & 0 & 0 & 0 & 0 & 0 \\ \frac{7}{2}S & 0 & -4e_xGS & -4e_yGS & 2T & 0 & 0 \\ 0 & 0 & 0 & 0 & 0 & 0 & 0 \end{bmatrix} \tag{7}$$

where the terms in the $\mathbf{A_{J2}}$ matrix are defined as in the following expressions:

$$\eta = \sqrt{1-e_c^2}, \quad \kappa_{J2} = \tfrac{3}{4}\tfrac{J_2R_E^2\sqrt{\mu}}{a^{3.5}\eta^4},$$
$$E = 1+\eta, \quad F = 4+3\eta, \quad G = \tfrac{1}{\eta^2}, \quad P = 3\ \cos^2(i_c)-1,$$
$$Q = 5\ \cos^2(i_c)-1, \quad S = \sin(2i_c), \quad T = \sin^2(i_c)$$

In a drag-free environment, a smart design of J2-invariant orbits allows to maintain the formation geometry with collision-free motion for hundreds of orbits with no additional station keeping (Morgan et al., 2012). That is why the majority of current research is focused on formation reconfiguration between invariant orbits, rather than formation maintenance for extended periods of time.

2.3. Atmospheric drag

One of the scopes of this work is to propose a guidance and control strategy for formation control in an environment in which drag effects are dominant and must be considered in the dynamics. In presence of drag, relative and absolute formation maintenance becomes mandatory, as also invariant relative bounded orbits will start drifting and decaying over time if uncontrolled. Different techniques have been proposed in recent research to include the effect of differential drag on Relative Orbital Elements in the propagation by defining a proper state transition matrix (Gaias et al., 2015; Koenig et al., 2017). In this paper a novel approach to derive a plant matrix is proposed, under the following assumptions:

- Control is assumed to be performed with respect to a non-decaying orbiting point, in order to perform relative transfers while maintaining the desired orbit altitude. Therefore, the chief is assumed to have a null ballistic coefficient and the ΔB term in the state vector will be equal to 1.
- The difference between absolute velocity in the Earth-Centered Inertial (ECI) frame and velocity relative to the atmosphere is negligible. Thus, the perturbing acceleration due to the presence of drag is purely tangential.

Under these simplifications, the time variations of relative semi-major axis and components of the relative eccentricity vector due to the presence of drag reduce to:

$$\begin{cases} \delta\dot{a} = \frac{\dot{a}}{a_c} \\ \delta\dot{e}_x = \dot{e}\cdot\cos(\omega) - e\dot{\omega}\cdot\sin(\omega) \\ \delta\dot{e}_y = \dot{e}\cdot\sin(\omega) + e\dot{\omega}\cdot\cos(\omega) \end{cases} \tag{8}$$

while other ROE are not influenced by the presence of drag. The effect of atmospheric drag on semi-major axis and eccentricity of the deputy satellites can then be retrieved from Gauss Variational Equations (GVE) (Battin, 1999) as:

$$\begin{cases} \dot{a} = \frac{2a^2v}{\mu}\cdot u_{drag} \\ \dot{e} = \frac{2(e+\cos(\theta))}{v}\cdot u_{drag} \\ \dot{\omega} = \frac{2\sin(\theta)}{ev}\cdot u_{drag} \end{cases} \tag{9}$$

in which the drag disturbance acceleration u_{drag} is expressed with a cannonball model as:

$$u_{drag} = \frac{1}{2}B\rho v^2 \tag{10}$$

where $B = \frac{C_D A}{m}$ is the deputy spacecraft ballistic coefficient, ρ is the atmospheric density computed with any model of choice, and v is the module of the velocity in the Earth-Centered Inertial frame. By correctly arranging these expressions, the resulting drag plant matrix $\mathbf{A_{drag}}$ can then be retrieved as:

$$\mathbf{A_{drag}} = B\rho v^2 \cdot \begin{bmatrix} 0 & 0 & 0 & 0 & 0 & 0 & \frac{a^2 v}{\mu} \\ 0 & 0 & 0 & 0 & 0 & 0 & 0 \\ 0 & 0 & 0 & 0 & 0 & 0 & \frac{(e+\cos(\theta))\cdot\cos(\omega)-\sin(\theta)\sin(\omega)}{v} \\ 0 & 0 & 0 & 0 & 0 & 0 & \frac{(e+\cos(\theta))\cdot\sin(\omega)+\sin(\theta)\cos(\omega)}{v} \\ 0 & 0 & 0 & 0 & 0 & 0 & 0 \\ 0 & 0 & 0 & 0 & 0 & 0 & 0 \\ 0 & 0 & 0 & 0 & 0 & 0 & 0 \end{bmatrix} \tag{11}$$

2.4. Drag plant matrix validation

The previously derived plant matrix is validated against the numerical results obtained with an orbital propagator considering only the effects of earth geopotential and drag, in order to isolate their influence. In particular, the errors in the components of the ROE state are retrieved and compared to the ones computed with a plant matrix which only includes the effects of J2 and Keplerian motion. The validation is performed for an integration time of five orbital periods both for a circular and for a highly eccentric orbit with low altitudes of perigee, to check for the generality of the model. To simulate atmospheric drag, the JB2008 model developed by Bowman et al. (2008) is employed. The starting osculating orbital elements of the selected orbits are reported in Table 1. The properties of the propagated satellites are listed in Table 2. Simulations start on 21st March 2015 at midnight. The results of the simulations are reported in Figs. 2 and 3. In both cases, it is possible to observe that, using the plant matrix including the drag effect, considerably higher accuracy is obtained for all ROE, along-track separation in particular.

Despite the assumption of null ballistic coefficient of the chief, useful for this specific application to follow a non-decaying reference, the derived matrix could be also used to represent relative motion with respect to a real spacecraft by selecting a proper value for ΔB. This parameter can be computed with simulations on ground if the physical properties of the chief and deputy satellites are known, extrapolated from flight data, or even estimated on-board with sequential nonlinear filtering techniques. The inclusion of ΔB estimation in the loop could be an interesting direction for further analyses.

Table 1
Starting orbital elements of the orbits used in the drag plant matrix validation.

Orbit	a [km]	e [-]	i [°]	Ω [°]	ω [°]
LEO	6771	0.001	97	30	90
HEO	16928	0.6	63.4	120	270

Table 2
Properties of the propagated satellites to validate the drag plant matrix.

	Chief	Deputy
Mass [kg]	20	20
C_D	-	2.1
Area [m^2]	0.1	0.1
B [m^2/kg]	-	0.0105
C_R [-]	1	1

2.5. Control input

In order to map the control accelerations in the LVLH reference frame into their effect on the ROE variation, the so-called control matrix **B** must be defined. For quasi-nonsingular ROE the expression is the one reported by Steindorf et al. (2017) and reported in the following:

$$\mathbf{B} = \frac{1}{a_c n_c} \cdot \begin{bmatrix} \frac{2}{\eta} e_c \sin(\theta_c) & \frac{2}{\eta}(1+e_c\cos(\theta_c)) & 0 \\ -\frac{2\eta^2}{1+e_c\cos(\theta_c)} & 0 & 0 \\ \eta\cdot\sin(u_c) & \eta\frac{(2+e_c\cos(\theta_c))\cos(u_c)+e_x}{1+e_c\cos(\theta_c)} & \frac{\eta e_y}{\tan(i_c)}\frac{\sin(u_c)}{1+e_c\cos(\theta_c)} \\ -\eta\cdot\cos(u_c) & \eta\frac{(2+e_c\cos(\theta_c))\sin(u_c)+e_y}{1+e_c\cos(\theta_c)} & -\frac{\eta e_x}{\tan(i_c)}\frac{\sin(u_c)}{1+e_c\cos(\theta_c)} \\ 0 & 0 & \eta\frac{\cos(u_c)}{1+e_c\cos(\theta_c)} \\ 0 & 0 & \eta\frac{\sin(u_c)}{1+e_c\cos(\theta_c)} \\ 0 & 0 & 0 \end{bmatrix} \tag{12}$$

2.6. Mean Orbital Elements propagation

Along with the propagation of ROE, a linear propagation of Mean Orbital Elements is necessary to compute the updated plant and control matrices at each time step, according to the orbit shape. The analytic propagation in performed by considering Keplerian motion and J2 secular effects on Ω, ω and M.

3. Model Predictive Control implementation

Model Predictive Control (MPC) is a modern control technique merging the advantages of optimal and feedback control. First, the controller exploits the knowledge of the system dynamics to solve an Optimal Control Problem (OCP) over a specified period of time defined as prediction horizon, discretized according to a selected sampling step. Once the optimization is completed, the resulting control is applied for a number of time steps defined by the so-called control horizon, then the optimisation starts again taking as initial condition the new observed state of the system. MPC was chosen as the guidance and control technique for the easy implementation of constraints and easy handling of multi-input multi-output (MIMO) systems. Its basic implementation is shown in Fig. 4.

Unlike open-loop optimal guidance, the dynamic feedback nature of Model Predictive Control makes the algorithm effective in compensating the inaccuracies of the

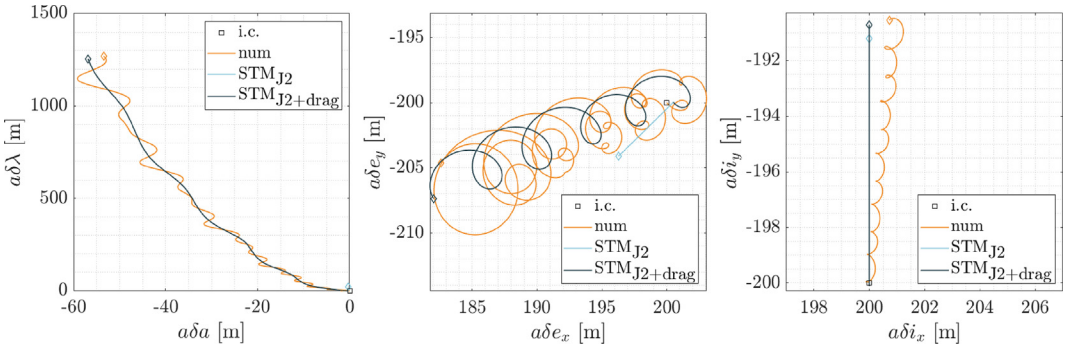

Fig. 2. Results of the drag matrix validation for a circular LEO. The state evolution is represented in terms of ROE over the simulation time of five orbits for the two cases of analytical propagation with and without drag plant matrix, compared to numerical integration.

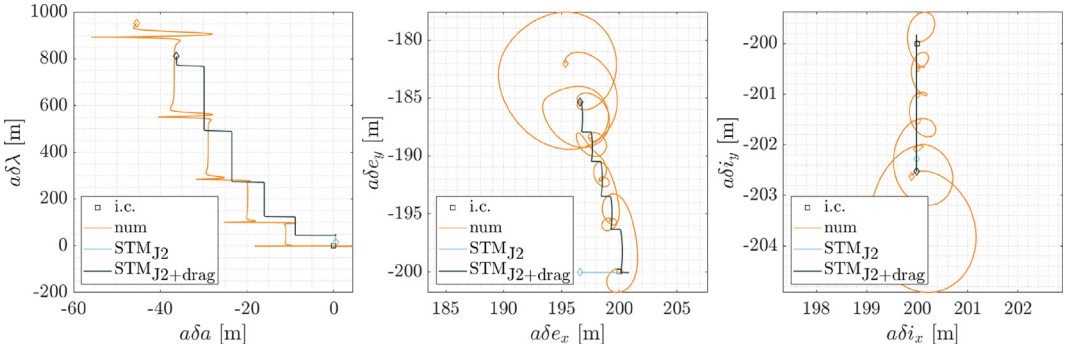

Fig. 3. Results of the drag matrix validation for a HEO with low perigee. The state evolution is represented in terms of ROE over the simulation time of five orbits for the two cases of analytical propagation with and without drag plant matrix, compared to numerical integration.

implemented model of the dynamics and even disturbances that are not included. However, a good model improves both the accuracy and fuel efficiency of the resulting trajectory.

3.1. Optimal Control Problem convexification

The main drawback of Model Predictive Control is the computational time needed to solve the optimal control problem at each time step. This is why an analytic model is used in the first place. In addition, the optimization cost function and constraints can be convexified in order to take advantage of convex optimization solvers, obtaining a fast and efficient solution viable for autonomous control. To write the optimal control problem in convex form, the first step is to discretize it. Following the procedure described by Morgan et al. (2014), time is divided into finite steps defined by the Model Predictive Controller sampling time, representing the sample interval for the state $\underline{\mathbf{x}}$ and the update interval for the control term $\underline{\mathbf{u}}$, which is considered piecewise constant for each time step.

Linear dynamics: The linear formulation of Eq. (4) is first discretized into a finite differences equation:

$$\underline{\mathbf{x}}_{\mathbf{j}}[k+1] = (\mathbf{A}[k]\Delta t + \mathbf{I})\ \underline{\mathbf{x}}_{\mathbf{j}}[k] + \mathbf{B}[k]\Delta t\ \underline{\mathbf{u}}_{\mathbf{j}}[k] \tag{13}$$

Then dynamics can be expressed as a linear equality constraint by defining a proper optimization vector containing not only the control input, but also the augmented ROE state at each time step. In particular, for each satellite it is defined a vector $\hat{\underline{\mathbf{x}}}_{\mathbf{j}}$ which contains the ROE state and the control input at each time instant k. $\hat{\underline{\mathbf{x}}}_{\mathbf{j}}$ has size $M = 7K + 3(K-1)$, where K is the total number of time steps. Subsequently, the entire decisional vector of the optimisation problem can be defined as:

$$\widehat{\underline{\mathbf{X}}} = \left(\hat{\underline{\mathbf{x}}}_{\mathbf{1}}, \ldots, \hat{\underline{\mathbf{x}}}_{\mathbf{j}}, \ldots, \hat{\underline{\mathbf{x}}}_{\mathbf{N}}\right)^T \tag{14}$$

with size $N \cdot M$, where N is the number of chaser satellites in the formation. Following the work by Sarno et al. (2020) and Scala et al. (2021), this formulation allows to rewrite the dynamics of each spacecraft in Eq. (13) in matrix form by defining a proper matrix $\mathbf{A}_{\mathbf{sd}}$ so that for each satellite it yields:

$$\mathbf{A}_{\mathbf{sd}} \cdot \hat{\underline{\mathbf{x}}}_{\mathbf{j}} = 0 \tag{15}$$

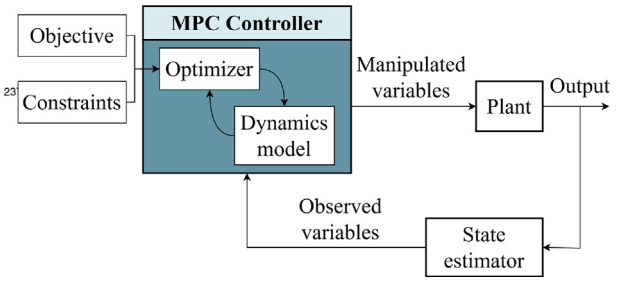

Fig. 4. Model Predictive Control loop.

where each row of $\underline{\mathbf{A}}_{\mathbf{sd}}$ is defined as:

$$\left[\mathbf{0}_{7\times 7(k-1)} \quad -(\mathbf{I} + \mathbf{A}[k]\Delta t) \quad \mathbf{I} \quad \mathbf{0}_{7\times 7K-4k-10} \quad -\mathbf{B}[k]\Delta t \quad \mathbf{0}_{7\times 3(K-k-1)}\right] \tag{16}$$

with $k = 1, \ldots, K$. Accordingly, the dynamics of the entire formation expressed in convex form as a linear equality constraint can be written as:

$$\widehat{\mathbf{A}}_{\mathbf{sd}} \cdot \widehat{\underline{\mathbf{X}}} = 0 \tag{17}$$

where:

$$\widehat{\mathbf{A}}_{\mathbf{sd}} = \begin{bmatrix} \cdots & \cdots & \cdots \\ \mathbf{0}_{7(K+1)\times M(j-1)} & \mathbf{A}_{\mathbf{sd}} & \mathbf{0}_{7(K+1)\times M(N-j)} \\ \cdots & \cdots & \cdots \end{bmatrix} \tag{18}$$

with $j = 1, \ldots, N$.

Initial and final conditions: Similarly, the initial and final state of each chaser satellite can be extracted from the decisional vector by defining the matrices $\mathbf{A}_{\mathbf{IC_j}}$ and $\mathbf{A}_{\mathbf{FC_j}}$.

$$\begin{cases} \delta\underline{\boldsymbol{\alpha}}_{\mathbf{j}}^{\mathbf{0}} = \mathbf{A}_{\mathbf{IC_j}} \cdot \hat{\underline{\mathbf{x}}}_{\mathbf{j}} = \begin{bmatrix} \mathbf{I}_7 & \cdots \\ \cdots & \mathbf{0}_{M-7} \end{bmatrix} \cdot \hat{\underline{\mathbf{x}}}_{\mathbf{j}} \\ \delta\underline{\boldsymbol{\alpha}}_{\mathbf{j}}^{\mathbf{F}} = \mathbf{A}_{\mathbf{FC_j}} \cdot \hat{\underline{\mathbf{x}}}_{\mathbf{j}} = \begin{bmatrix} \mathbf{0}_{7K-7} & \cdots & \cdots \\ \cdots & \mathbf{I}_7 & \cdots \\ \cdots & \cdots & \mathbf{0}_{3(K-1)} \end{bmatrix} \cdot \hat{\underline{\mathbf{x}}}_{\mathbf{j}} \end{cases} \tag{19}$$

This formulation can again be extended to all satellites in the formation by defining:

$$\begin{cases} \mathbf{A}_{\mathbf{IC}} = \begin{bmatrix} \cdots & \cdots & \cdots \\ \mathbf{0}_{M\times M(j-1)} & \mathbf{A}_{\mathbf{IC_j}} & \mathbf{0}_{M\times M(N-j)} \\ \cdots & \cdots & \cdots \end{bmatrix} \\ \mathbf{A}_{\mathbf{FC}} = \begin{bmatrix} \cdots & \cdots & \cdots \\ \mathbf{0}_{M\times M(j-1)} & \mathbf{A}_{\mathbf{FC_j}} & \mathbf{0}_{M\times M(N-j)} \\ \cdots & \cdots & \cdots \end{bmatrix} \end{cases} \tag{20}$$

so that:

$$\begin{cases} \delta\underline{\boldsymbol{\alpha}}^{\mathbf{0}} = \mathbf{A}_{\mathbf{IC}} \cdot \widehat{\underline{\mathbf{X}}} \\ \delta\underline{\boldsymbol{\alpha}}^{\mathbf{F}} = \mathbf{A}_{\mathbf{FC}} \cdot \widehat{\underline{\mathbf{X}}} \end{cases} \tag{21}$$

Cost function: The cost functional to be minimized in the OCP must be expressed in terms of the discretized decisional vector $\widehat{\underline{\mathbf{X}}}$ as well. Hence, also the control term must be isolated. In particular, a matrix $\widehat{\mathbf{H}}$ can be defined so that:

$$\widehat{\underline{\mathbf{U}}} = \widehat{\mathbf{H}} \cdot \widehat{\underline{\mathbf{X}}} \tag{22}$$

where the $\widehat{\underline{\mathbf{U}}}$ vector contains the control accelerations in their respective position and is equal to zero in its other components. By defining the weighting matrices $\mathbf{P}$ and $\mathbf{Q}$, the cost function is then expressed as:

$$J = ||\widehat{\mathbf{H}} \cdot \widehat{\underline{\mathbf{X}}}||_1 + ||\mathbf{P}\left(\mathbf{A}_{\mathbf{FC}} \cdot \widehat{\underline{\mathbf{X}}} - \widehat{\underline{\mathbf{X}}}_{\mathbf{T}}\right)||_1 + ||\mathbf{Q}\left(\widetilde{\underline{\mathbf{X}}} - \widetilde{\underline{\mathbf{X}}}_{\mathbf{T}}\right)||_1 \tag{23}$$

Namely:

- $||\widehat{\mathbf{H}} \cdot \underline{\widehat{\mathbf{X}}}||_1$ is the control effort term, added to minimize the propellant consumption finding a sub-optimal fuel efficient solution.
- $||\mathbf{P}\left(\mathbf{A_{FC}} \cdot \underline{\widehat{\mathbf{X}}} - \underline{\widehat{\mathbf{X}}}_{\mathbf{T}}\right)||_1$ is the tracking error of the final state with respect to the target ROE vector. Its minimization leads to the convergence of the state to the desired one.
- $||\mathbf{Q}\left(\underline{\widetilde{\mathbf{X}}} - \underline{\widetilde{\mathbf{X}}}_{\mathbf{T}}\right)||_1$ identifies the difference between the target ROE vector and the ROE state of the satellites at each time step. The introduction of this expression speeds up the convergence towards the target system state and avoids excessive deviations from the reference trajectory.

Since the cost function is a sum of 1-norms, it is convex and also linear. Moreover, the introduction of tracking terms in the objective, rather than as a hard constraint on the final target, ensures the feasibility and also the convergence of the problem, if these terms are weighted enough. The choice of proper weighting matrices allows to prioritize or even isolate the tracking error relative to some Relative Orbital Elements with respect to others, depending on the scenario. The chosen values strongly depend on mission requirements, thus, their selection differs from case to case. However, two general considerations that must be taken into account are that the tracking errors should be weighted enough to make the spacecraft converge to the desired state, as anticipated previously, and that the higher the weights on tracking error terms, the quicker the transfer will be. This last characteristic can be exploited in particular operational situations where timeliness is crucial.

3.2. Actuation constraints

Thrust module constraint: The constraints added in the control problem to obtain a feasible control profile are strongly linked to the available propulsion solution, a single low-thrust engine in this case. In current research on relative dynamics, guidance, and control, it is often assumed that the spacecraft is capable of thrusting in any direction at any time. This is however rarely true, in particular when employing electric engines, unless the satellite is equipped with attitude thrusters that can be also used for orbit control. Dealing with a single engine, the constraint on the maximum acceleration is given on the module rather than for each component. This is achieved by isolating and reshaping the control at each time step k for each satellite j from the decisional vector $\underline{\widehat{\mathbf{X}}}$. Then, it is enough to impose that the norm of the control acceleration vector is lower than the maximum acceleration that the engine is able to provide to the spacecraft at each time step for each satellite:

$$\begin{aligned} &||\underline{\mathbf{u}}_j^k||_2 \leqslant \tfrac{T_{max}}{m_{s/c}}, \\ &k = 1, \ldots, K, \quad j = 1, \ldots, N \end{aligned} \tag{24}$$

Most of low-thrust propulsion units also have a limit in the lowest thrust they are able to provide. This constraint is impossible to express in convex form, as it would represent a "hole" in the hyper-dimensional space. Therefore this constraint can only be imposed a posteriori on the minimization results, just by ignoring control actions that have a norm lower than the minimum acceleration of the engine. The algorithm will compensate by providing a higher control action at a later time, converging anyway to the target.

Radial thrust: As along-track separation $\delta\lambda$ can be controlled by acting on the relative semi-major axis, all in-plane ROE can be controlled effectively by only applying a tangential thrust. Therefore, radial thrust could be set to zero a priori in order to obtain a simpler solution. This constraint can be included in the algorithm just by isolating the radial control components of the decisional vector and imposing the equality to zero. Furthermore, setting the radial thrust to null greatly simplifies the inclusion of constraints on thrusting angles in convex form.

Constraints on thrust angles and slew rates: During nominal operations of the spacecraft, having only one available propulsive unit, additional constraints should be imposed on the thrusting angle and on the maximum allowed slew rate to point the engine in the desired direction. For example, a thrust cone constraint may be included for orbit maintenance, trying to maintain the attitude as close as possible to earth-pointing in order to be ready for observation. On the other hand, a slew rate limit may be imposed for formation reconfiguration maneuvers, which may ask for a too quick and unfeasible redirecting of the thrust vector. The in-plane and off-plane thrusting angles are defined according to the spherical coordinates representation shown in Fig. 5. In particular, the in-plane angle ϕ is defined starting from the T axis, which is coincident with the along-track direction for circular orbits, and taken positive in anticlockwise direction. On the other hand, the off-plane angle θ is the angle between $\underline{\mathbf{u}}$ and the RT plane. These are defined in degrees as:

$$\begin{cases} \phi = \arctan\left(\frac{u_y}{u_x}\right) - 90^\circ \\ \theta = \arcsin\left(\frac{u_z}{u}\right) \end{cases} \tag{25}$$

The angle ϕ is defined from 0° to 360°, whereas θ is defined from -90° to 90°. Including the radial thrust constraint, the angle ϕ can only assume precisely a value of 0° or 180°. Therefore, a constraint on the in-plane angle can simply be included on the sign of the u_y component. On the other hand, the constraint on the maximum off-plane angle θ is imposed as:

$$|\underline{\mathbf{u}}_\mathbf{z}| \leqslant |\underline{\mathbf{u}}_\mathbf{y}| \cdot \tan(\theta_{max}) \tag{26}$$

The inclusion of a constraint on the maximum slewing rate is not natural in convex form, due to the tight restrictions imposed by convex programming. The most basic

idea consists in imposing a maximum difference between the components of the control vector at a given time step k and the same component at time $k+1$. The first obvious drawback of this strategy is that the same difference corresponds to different angles depending on the control vector module, until the introduction of the constraint becomes irrelevant for very small controlling accelerations. However, this effect is mitigated by the inclusion of the minimum thrust threshold explained before, which, if high enough, may be exploited for the inclusion of the slew constraint. Another undesired effect is that this type of check interprets the engine switch-off as a slew, due to the sudden variation of control components. Despite all these stringent limitations, a procedure is found to at least deny the presence of immediate sign changes for each axis. Assuming a null radial thrust constraint, this consists in imposing:

$$\begin{cases} |u_y^{k+1} - u_y^k| \leqslant a_{max} \\ |u_z^{k+1} - u_z^k| \leqslant a_{max} \end{cases} \tag{27}$$

With this expression, if a minimum thrust limit higher than half of the maximum value is added, engine switch-offs are allowed, but at the same time sudden 180° slews are impossible. Indeed, at least a time step with no control is mandatory before switching the control sign of each component. This control-free step can be used to slew in the desired direction with enough time to perform a feasible maneuver, as the MPC sampling time is chosen in the order of the hundreds of seconds. If one time step is not enough to safely perform the slew in time, the previous formulation just needs to be extended also to the $k+2$ step and so on, according to the mission specifications and requirements. Additional constraints may be added to cover slews between different axes. An example of constraint for normal and tangential maneuver splitting can be imposed as:

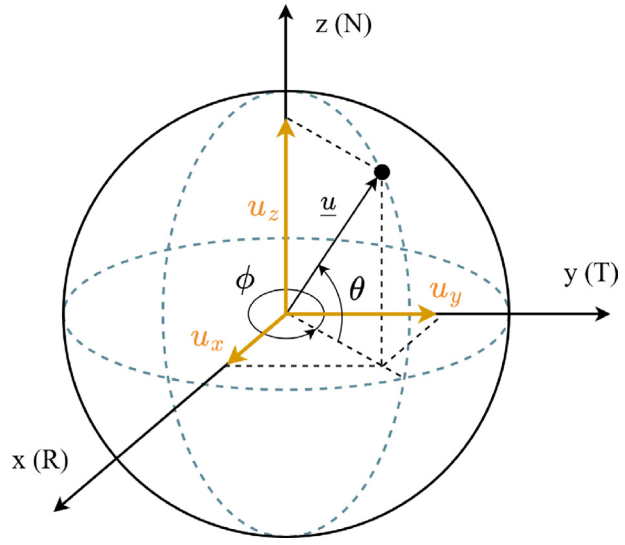

Fig. 5. Spherical coordinates reference frame for the control vector.

$$\begin{cases} |u_y^{k+1}| + |u_z^k| \leqslant a_{max} \\ |u_z^{k+1}| + |u_y^k| \leqslant a_{max} \end{cases} \tag{28}$$

Naturally, this constraint does not deny impossible slews in all situations. In any case, in a real application, if the spacecraft is not able to perform a manoeuvre in time due to the saturation of attitude control actuators, the feedback behaviour of the MPC will compensate in future re-iterations, taking more time but converging to the target.

3.3. Collision avoidance

Collision avoidance must be imposed as an inequality constraint on the relative position of the satellites in the formation in the LVLH frame. Since the state vector is expressed in ROE form, a linear transformation is needed to retrieve the xyz coordinates before imposing collision avoidance. The selected linear mapping, represented by the matrix $\mathbf{T}$, is derived following the procedure reported by Silvestrini and Lavagna (2021), but neglecting the velocity components, which are not necessary for the collision avoidance algorithm. Also the seventh element of the state, the differential ballistic coefficient, is not needed and therefore is discarded.

$$\underline{\mathbf{x}}_{\mathbf{LVLH}} = \begin{pmatrix} x \\ y \\ z \\ 0 \\ 0 \\ 0 \\ 0 \end{pmatrix} = \mathbf{T} \cdot \boldsymbol{\delta}\underline{\boldsymbol{\alpha}} \tag{29}$$

The transformation matrix $\mathbf{T}$ is derived by using an intermediate change of coordinates exploiting the classical orbital elements differences vector $\Delta OE = [\Delta a, \Delta M, \Delta\omega, \Delta e, \Delta i, \Delta\Omega]$ as follows:

$$\mathbf{T} = \frac{\partial \underline{\mathbf{x}}_{\mathbf{LVLH}}}{\partial \Delta OE} \cdot \frac{\partial \Delta OE}{\partial \boldsymbol{\delta}\underline{\boldsymbol{\alpha}}} \tag{30}$$

The first-order approximation of the mapping between the LVLH state and classical osculating orbital elements difference is taken from equations derived by D'Amico (2010):

$$\begin{cases} x = \frac{r}{a}\Delta a - a \cdot \cos(\theta)\Delta e + \frac{a \cdot e \cdot \sin(\theta)}{\sqrt{1-e^2}}\Delta M \\ y = \left(a + \frac{r}{1-e^2}\right)\sin(\theta)\Delta e + \frac{a^2}{r}\eta\Delta M + r\Delta\omega \; + \; r \cdot \cos(i)\Delta\Omega \\ z = r \cdot \sin(u)\Delta i - r \cdot \sin(i)\cos(u)\Delta\Omega \end{cases} \tag{31}$$

From the previous equations, the first transformation matrix can be retrieved. Since only the relative positions are of interest, the last four rows can be set equal to zero

to avoid useless computations. The same yields for the last column, as no dependence on the differential ballistic coefficient is present.

$$\frac{\partial \underline{\mathbf{x}}_{\mathbf{LVLH}}}{\partial \Delta OE} = r \cdot \begin{bmatrix} 1/a & \frac{a \cdot e \cdot \sin(\theta)}{r\sqrt{1-e^2}} & 0 & -\frac{a}{r} \cdot \cos(\theta) & 0 & 0 & 0 \\ 0 & \frac{a^2}{r^2}\eta & 1 & \left(\frac{a}{r} + \frac{1}{1-e^2}\right)\sin(\theta) & 0 & \cos(i) & 0 \\ 0 & 0 & 0 & 0 & \sin(u) & -\sin(i)\cos(u) & 0 \\ 0 & 0 & 0 & 0 & 0 & 0 & 0 \\ 0 & 0 & 0 & 0 & 0 & 0 & 0 \\ 0 & 0 & 0 & 0 & 0 & 0 & 0 \\ 0 & 0 & 0 & 0 & 0 & 0 & 0 \end{bmatrix} \tag{32}$$

In order to obtain the full mapping, the Jacobian of the transformation from classical orbital elements to quasi-nonsingular ROE is necessary. This is obtained from the definition of $\boldsymbol{\delta}\underline{\boldsymbol{\alpha}}$ for $\delta OE \rightarrow 0$ as:

$$\frac{\partial \Delta OE}{\partial \boldsymbol{\delta}\underline{\boldsymbol{\alpha}}} = \begin{bmatrix} a & 0 & 0 & 0 & 0 & 0 & 0 \\ 0 & 1 & \frac{\sin(\omega)}{e} & -\frac{\cos(\omega)}{e} & 0 & \frac{\cos(i)}{\sin(i)} & 0 \\ 0 & 0 & -\frac{\sin(\omega)}{e} & \frac{\cos(\omega)}{e} & 0 & 0 & 0 \\ 0 & 0 & \cos(\omega) & \sin(\omega) & 0 & 0 & 0 \\ 0 & 0 & 0 & 0 & 1 & 0 & 0 \\ 0 & 0 & 0 & 0 & 0 & \sin(i) & 0 \\ 0 & 0 & 0 & 0 & 0 & 0 & 0 \end{bmatrix} \tag{33}$$

Multiplying the two matrices, the complete transformation matrix $\mathbf{T}$ isolating relative positions in the LVLH frame is retrieved. To impose collision avoidance on the full optimization decisional vector $\widehat{\underline{\mathbf{X}}}$, the matrix $\mathbf{T}[k]$ needs to be evaluated at each time step to form the matrix $\widehat{\mathbf{T}}_{\mathbf{j}}$, defined for the j-th satellite as follows:

$$\widehat{\mathbf{T}}_{\mathbf{j}} = \begin{bmatrix} \begin{bmatrix} \cdots & \cdots & \cdots \\ \mathbf{0}_{7\times 7(k-1)} & \mathbf{T}[k] & \mathbf{0}_{7\times 7(K-k)} \\ \cdots & \cdots & \cdots \end{bmatrix} & \mathbf{0}_{7K\times 3(K-1)} \\ \mathbf{0}_{3(K-1)\times 7K} & \mathbf{0}_{3(K-1)} \end{bmatrix} \tag{34}$$

As for other previously derived matrices, the matrix for the entire formation can be assembled by properly rearranging the matrices $\widehat{\mathbf{T}}_{\mathbf{j}}$ in a larger matrix $\widehat{\mathbf{T}}$:

$$\widehat{\mathbf{T}} = \begin{bmatrix} \cdots & \cdots & \cdots \\ \mathbf{0}_{M\times M(j-1)} & \widehat{\mathbf{T}}_{\mathbf{j}} & \mathbf{0}_{M\times M(N-j)} \\ \cdots & \cdots & \cdots \end{bmatrix} \tag{35}$$

Once the x, y, and z components of the decisional vector of each satellite are isolated, it is necessary to impose the minimum distance constraint in a formulation suitable for convex programming. The selected methodology is the one introduced by Morgan et al. (2014). This strategy consists in generating separating planes among the satellites, transforming the circular prohibited zone into a suitable convex formulation. A graphical representation of the convexified constraint is reported in Figs. 6 and 7. It can be observed that the convexified prohibited zone contains entirely the nonconvex one, this means that collision avoidance is guaranteed. Morgan's formulation states that, at each time instant k, the following inequality must be satisfied between each i/j spacecraft couple in the formation:

$$\begin{aligned} &\left(\bar{\underline{\boldsymbol{\chi}}}_j[k] - \bar{\underline{\boldsymbol{\chi}}}_i[k]\right)^T \mathbf{C}^T \mathbf{C}\left(\underline{\boldsymbol{\chi}}_j[k] - \underline{\boldsymbol{\chi}}_i[k]\right) \\ &\quad \geqslant d_{thr} ||\mathbf{C}\left(\bar{\underline{\boldsymbol{\chi}}}_j[k] - \bar{\underline{\boldsymbol{\chi}}}_i[k]\right)||_2 \end{aligned} \tag{36}$$

where the solution vectors $\boldsymbol{\chi}$ are expressed in cartesian coordinates in the LVLH frame, $\bar{\boldsymbol{\chi}}$ represents an initial guess of the optimal trajectory followed by the spacecraft, and $\mathbf{C}$ is a matrix built to isolate only the position components of the solution. This expression must be reformulated to deal with quasi-nonsingular ROE, exploiting the previously introduced linear mapping, and with the entire decisional vector $\widehat{\underline{\mathbf{X}}}$. As explained previously, the linear mapping matrix $\widehat{\mathbf{T}}$ is built to already isolate the positional components of the LVLH frame. Therefore, the right term of Eq. (36) can be rewritten for each time step k as:

$$d_{thr} ||\mathbf{C}\left(\bar{\underline{\boldsymbol{\chi}}}_j[k] - \bar{\underline{\boldsymbol{\chi}}}_i[k]\right)||_2 = d_{thr} ||\mathbf{T}[k] \cdot \left(\bar{\underline{\mathbf{x}}}_j[k] - \bar{\underline{\mathbf{x}}}_i[k]\right)||_2 \tag{37}$$

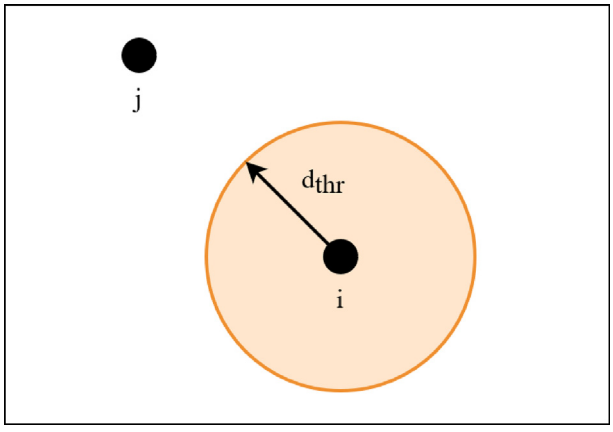

Fig. 6. Nonconvex collision avoidance constraint.

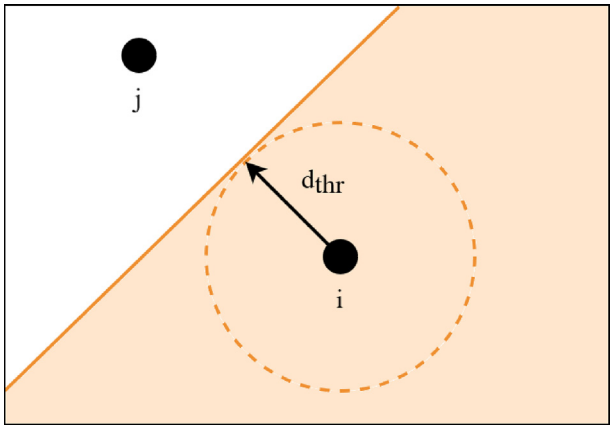

Fig. 7. Convexified collision avoidance constraint (Morgan et al., 2014).

In order to deal with all time steps at once, i.e. to deal with the entire decisional vector, this expression must be generalized by defining a proper vector $\underline{\mathbf{d}}_{CA}$, built by taking the norm of difference of the positional components in the LVLH frame of the initial guess vector at each time step.

$$\underline{\mathbf{d}}_{CA} = d_{thr} \cdot \begin{bmatrix} \cdots \\ ||\mathbf{T}[k] \cdot \left(\underline{\bar{\mathbf{x}}}_j[k] - \underline{\bar{\mathbf{x}}}_i[k]\right)||_2 \\ \cdots \end{bmatrix} \tag{38}$$

For the proposed algorithm, the initial guess is represented by a solution of the same problem obtained without imposing collision avoidance.

For what concerns the left term of Eq. (36), the left half concerning the guess vector can be rewritten in matrix form by correctly rearranging the differences in the positional components of the initial guess vector transformed in LVLH form, building a matrix $\overline{\mathbf{D}}$ as follows:

$$\overline{\mathbf{D}} = \begin{bmatrix} \cdots & \cdots & \cdots \\ \mathbf{0}_{1\times 3(k-1)} & \left[\bar{x}_j^k - \bar{x}_i^k,\ \bar{y}_j^k - \bar{y}_i^k,\ \bar{z}_j^k - \bar{z}_i^k\right] & \mathbf{0}_{1\times 3(K-k)} \\ \cdots & \cdots & \cdots \end{bmatrix} \tag{39}$$

On the other hand, the LVLH positional differences between two satellites of the formation can be isolated from the decisional vector $\widehat{\underline{\mathbf{X}}}$ defining a matrix $\widehat{\mathbf{A}}_{CA}$ as:

$$\widehat{\mathbf{A}}_{CA} = \begin{bmatrix} \cdots & \cdots & \cdots & \cdots & \cdots \\ \mathbf{0}_{3\times 7(k-1)} & \mathbf{I}_3 & \mathbf{0}_{3\times 2(5K-3)} & -\mathbf{I}_3 & \mathbf{0}_{3\times 10K-7k+1} \\ \cdots & \cdots & \cdots & \cdots & \cdots \end{bmatrix} \tag{40}$$

Finally, the reformulated expression for the convexified collision avoidance constraint to be implemented in the algorithm can be written for each satellite couple i/j as:

$$\overline{\mathbf{D}} \cdot \left(\widehat{\mathbf{A}}_{CA}\widehat{\mathbf{T}}\widehat{\underline{\mathbf{X}}}_{\mathbf{i/j}}\right) \geqslant \underline{\mathbf{d}}_{CA} \tag{41}$$

where $\widehat{\underline{\mathbf{X}}}_{\mathbf{i/j}}$ only contains the decisional vectors of the i-th and j-th satellites of the formation. The constraint ensures that the threshold distance is respected in the sample points of the optimization vector, but not between one sample and the following one. An analysis of the maximum crossing of the separating plane due to natural dynamics between two sampling steps could give a useful result to set a conservative threshold that takes this aspect into account.

Furthermore, the addition of the collision avoidance constraint may introduce a source of infeasibility in the problem, which may occur if the collision avoidance inequality clashes with the hard constraint on the initial condition. However, it is enough to impose a starting geometry in which all inter-satellite distances are larger than the CA threshold, then the MPC will guide the satellites to the target respecting the safety margin.

3.4. OCP implementation in the convex solver

Algorithm 1. Convex Optimization Problem in cvx

1: **cvx_begin**
2: *cvx_solver*: SeDuMi (or sdpt3)
3: *cvx_precision*: best
4: *variable*: $\widehat{\underline{\mathbf{X}}}(N \cdot M)$
5: *minimize*: $J = ||\widehat{\mathbf{H}} \cdot \widehat{\underline{\mathbf{X}}}||_1 + ||\mathbf{P}\left(\mathbf{A_{FC}} \cdot \widehat{\underline{\mathbf{X}}} - \widehat{\underline{\mathbf{X}}}_{\mathbf{T}}\right)||_1 + ||\mathbf{Q}\left(\widetilde{\underline{\mathbf{X}}} - \widetilde{\underline{\mathbf{X}}}_{\mathbf{T}}\right)||_1$
6: *subject to*:
7: $\widehat{\mathbf{A}}_{\mathbf{sd}} \cdot \widehat{\underline{\mathbf{X}}} = 0$
8: $\mathbf{A_{FC}} \cdot \widehat{\underline{\mathbf{X}}} = \widehat{\underline{\mathbf{X}}}_{\mathbf{0}}$
9: $||\underline{\mathbf{u}}_j^k||_2 \leqslant T_{max}/m_{s/c}$
10: $\overline{\mathbf{D}} \cdot \left(\widehat{\mathbf{A}}_{CA}\widehat{\mathbf{T}}\widehat{\underline{\mathbf{X}}}_{\mathbf{i/j}}\right) \geqslant \underline{\mathbf{d}}_{CA}$
11: [Thrust angles constraints, eq.(26)]
12: [Slew rate constraints, eq.(27), eq.(28)]

The problem is then implemented in a convex optimization solver as shown in Algorithm 1. The specific notation depends on the solver and on the language it operates on. For this study, `cvx 1.22` (Grant et al., 2008; Grant and Boyd, 2014) is used for simulations in MATLAB and the `CVXPY 1.1` library (Diamond and Boyd, 2016; Agrawal et al., 2018) is used for simulations performed using Python. In Algorithm 1 the generic MATLAB implementation in cvx form is shown with the two selected parameters of solver and precision. `cvx 1.22` currently supports two different solvers: SeDuMi (Sturm, 1999) and SDPT3 (Toh et al., 1999), with the first being the default and usually recommended option. The precision string argument allows to select the accuracy of the solution from a set of predefined precision models. For the proposed implementation `best` precision model is selected, setting the so-called solver target to zero. This means that the solver continues as long as it can make progress, producing more accurate solutions. Precision can be lowered if faster solutions are desired.

4. Validation

The validation of some key aspects of the algorithm is performed by integrating the control profile computed by the MPC with a high-fidelity propagator which is considered ground truth. The relative motion between the chief and deputies is obtained by integrating the agents separately, considering the perturbations acting on each spacecraft. In particular, the model considers the earth's geopotential up to the third zonal harmonic, atmospheric drag, solar radiation pressure (SRP), and third-body perturbations induced by the moon and the sun. The separated integration of the chief allows to consider only some

Table 3
Orbital elements of the orbit used for fuel efficiency validation (Catanoso et al., 2019).

a [km]	e [-]	i [rad]	Ω [°]	ω [°]	M_0 [°]
6828	0.00001	1.361	0	0	0

Table 4
Starting and target relative states used for fuel efficiency validation (Catanoso et al., 2019).

	$a\delta\underline{\alpha}$ [m]
i. c.	$[0, 0, 273, 0, 10, 70]$
f. c.	$[0, 0, 273, 0, 400, 120]$

desired perturbations, if any, in order to propagate the desired reference orbiting slot.

4.1. Fuel efficiency

The reliability and optimality of the designed control solution are verified by comparing it with other options available in the literature. A close match to the proposed strategy is the one developed by Catanoso et al. (2019), in which a Lyapunov-based MPC based on ROE dynamics is introduced. With respect to this reference, fuel efficiency is assessed by performing a comparison between the two MPC solutions of the same transfer and with the closed-form impulsive solution developed by Chernick and D'Amico (2018). Moreover, a solution obtained with a direct single shooting (DSS) method is added to the comparison to have an optimal low-thrust benchmark. The starting keplerian parameters of the orbit that was selected in the chosen reference are reported in Table 3, and the starting and target relative states are reported in Table 4.

The only information about the simulated spacecraft is the maximum acceleration that can be provided along each axis, which amounts to $3.2 \cdot 10^{-5}$ m/s^2. In the provided solution no tangential thrust is present, therefore the validation will be focused on the out-of-plane control, with both satellites propagated including drag effects, but left decaying together while completing the maneuver. The weights of the MPC cost function have been tuned in order to match the transfer time of the reference solution, corresponding to seven orbit periods. The resulting trajectory computed by the proposed MPC in the LVLH reference frame is shown in Fig. 8, whereas the computed control profile is reported in Fig. 9 together with the reference nonlinear counterpart. The resulting ΔV needed to complete the transfer with the desired accuracy is compared to the other results in Table 5.

The proposed solution demonstrates to be close to optimal, obtaining lower propellant consumption than the nonconvex reference and coming close to the single shooting and impulsive optimal solutions while being viable for on-board autonomous low-thrust control. In addition, the resulting control profile is feasible for an average micro-satellite mounting only one propulsive unit on-board, without unrealistic requirements on the agility of the satellite.

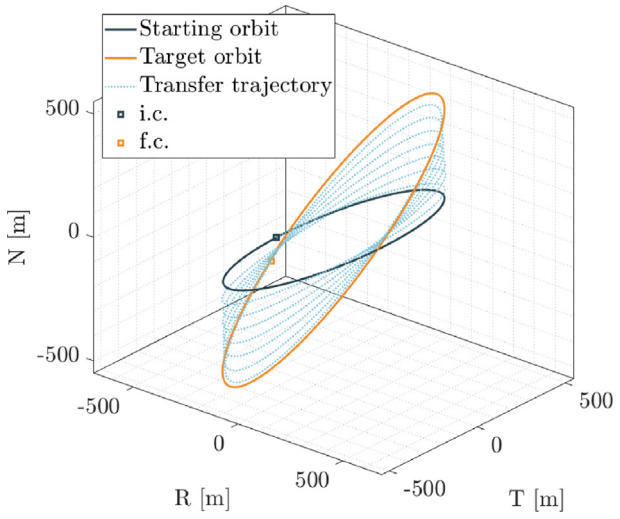

Fig. 8. Trajectory in the LVLH frame for the out-of-plane transfer used for fuel efficiency validation.

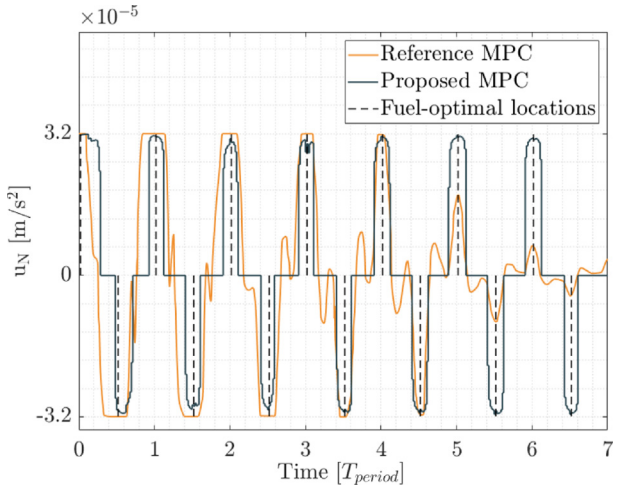

Fig. 9. Control acceleration in normal direction for the out-of-plane transfer. The reference used for comparison is taken from Catanoso et al. (2019).

Table 5
ΔV comparison between convex MPC, the two considered literature solutions, and direct single shooting.

Method	ΔV [m/s]
Reference MPC	0.5554
Proposed MPC	0.4931
Direct single shooting	0.4680
Closed-form impulsive	0.4373

4.2. Drag compensation

Due to the feedback nature of Model Predictive Control, it can be argued that the inclusion of a drag plant

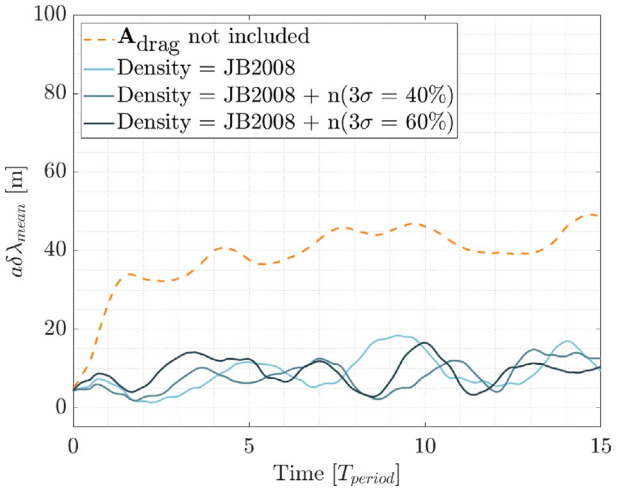

Fig. 10. Mean $a\delta\lambda$ evolution over one day of simulation for the four test cases.

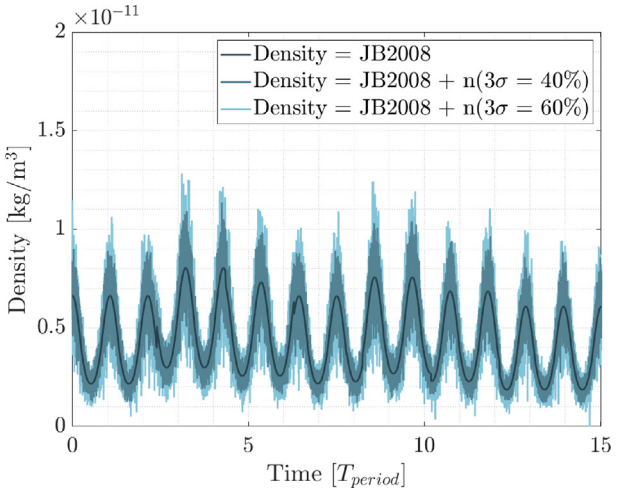

Fig. 11. Density evolution for the three test cases in which $\mathbf{A}_{\mathbf{drag}}$ is included.

matrix is not mandatory, as the relative drift would be corrected anyway by the MPC prescribing a tangential maneuver when an undesired along-track separation is created. To prove the effectiveness of the proposed drag model and justify its inclusion in the controller, the tracking of a holding point placed in the chief spacecraft's position is simulated. This equals to controlling the deputy spacecraft in its absolute dynamics to compensate for the effects of drag and to maintain its along-track position. By simulating with and without including the drag plant matrix in the dynamics propagation of the MPC, results can be compared and the effectiveness of the drag model can be assessed. In addition, the same case scenario is studied when a zero-mean gaussian noise n is added to the density value expected by the JB2008 density model, in order to check for the control accuracy in presence of a mismatch between the real density and the one predicted by the controller. The variation in time of $\delta\lambda$ and density for the different cases over one day of simulation are represented in Figs. 10 and 11. The mean along-track error is averaged over one orbit to retrieve its mean evolution. From the figures, it is evident that the inclusion of the plant matrix improves the accuracy of the solution in terms of tracking of the desired along-track separation. Indeed in both cases, a constant mean altitude is maintained, but, when drag is not considered in the propagation, a $\delta\lambda$ error of about 40 m is accumulated throughout the day and is never corrected even after running the simulation for more time. Furthermore, the results of the simulations are compared in terms of fuel optimality to the integration of the drag-induced acceleration over the simulation time span, amounting to about 0.11 m/s. The controller shows a close to fuel-optimal behavior both with and without including the drag plant matrix in the linear dynamics model, as reported in Table 6, with no unnecessary maneuvers to compensate for the energy decrease.

Table 6
Comparison of simulation results obtained for the validation of drag plant matrix effectiveness on control.

	$a\delta\lambda_{mean}$	ΔV
Without $\mathbf{A_d}$	38.69 m	~0.11 m/s
Density = JB	8.90 m	~ 0.11 m/s
Density = JB + $n(3\sigma = 40\%)$	7.98 m	~0.11 m/s
Density = JB + $n(3\sigma = 60\%)$	9.13 m	~0.11 m/s

The simulations show a $\delta\lambda$ error also when the drag plant matrix is included in the propagation, although considerably smaller and consistent for all three test cases, showing that a zero-mean gaussian error on the density knowledge has no major effect on control accuracy and efficiency. This error is to be attributed to the constraints introduced in the simulation, namely, a minimum thrust that can be provided by the engine, and limitations to avoid continuous firing and excessive slewing. These will be better discussed in the next section together with the controller parameters used for this and the following simulations.

5. Simulations

5.1. Simulation parameters

The MPC parameters have been chosen relying on generally suggested practices for MPC design, case-specific considerations, and simulation results. The selected values are reported in Table 7.

The recommended procedure to select the prediction horizon is to have it as large as possible until further increase brings small to no improvement to the controller performance. For the following simulations, this value is fixed to one orbital period, since longer horizons only have a negative impact on computational time. The sampling time of the MPC is set as 100 s, a good compromise between MPC accuracy and computational efficiency.

Table 7
Parameters of the Model Predictive Controller used in the simulations.

Parameter	Value
Prediction Horizon	5600 s
Sampling time, T_s	100 s
Control Horizon	$7 \cdot T_s$

Finally, the control horizon is set as seven sampling steps. This means that the on-board computer shall solve the optimal control problem about eight equidistant times for a LEO orbit at 400 km altitude. Naturally, a smaller control horizon improves the reactivity of the controller to unmodelled perturbances and promotes stability, but the selected recalculation frequency was found to be a good compromise to have a stable controller and achieve good control accuracy while limiting the computational burden on the hardware. To check the robustness and flexibility of the proposed controller, several different operational scenarios are simulated for both formation reconfiguration and maintenance, in which the satellites are also requested to maintain a constant orbit altitude throughout the maneuver. In particular, the algorithm is tested in representative or challenging but realistic conditions. For all simulations, the properties of the chasers are the ones reported in Table 8. According to the premises made in the introduction and along the paper, the simulated spacecraft are micro-satellites actuated by a single low-thrust engine with low authority and a minimum thrust threshold. in all simulations, the chief spacecraft is be propagated with a null ballistic coefficient, in order to represent a non-decaying orbiting reference point.

Also the orbit geometry is shared by all simulations unless specified. The chosen reference orbit is a low altitude Sun-synchronous orbit (SSO), to test the MPC performance in a high-drag environment which also represents a realistic choice for a scientific or earth observation mission in Low Earth Orbit. The selected orbital parameters

Table 8
Properties of chaser satellites used in all simulations.

Parameter	Value
Mass	20 kg
Drag area	0.1 m^2
C_D	2.1
SRP area	0.1 m^2
C_R	1
Max thrust	0.65 mN
Min thrust	0.35 mN

Table 9
Starting osculating orbital elements of the reference orbit used in the simulations.

a [km]	e [-]	i [°]	Ω [°]	ω [°]	M_0 [°]
6771	0.001	97.004	30	90	0

Table 10
Starting and target relative states for the relative eccentricity change.

	$a\delta\underline{\alpha}$ [m]
i. c.	[0, 0, 0, 400, 0, 400]
f. c.	[0, 0, 0, 200, 0, 400]

are reported in Table 9. All simulations start on 21st March 2015 at midnight.

5.2. Relative eccentricity change

The first simulated scenario is a change of relative eccentricity. The starting and target relative states for this reconfiguration are reported in Table 10, in both cases eccentricity/inclination vector separation is guaranteed. This concept, originally developed for GEO satellites, is used to impose a passive collision avoidance constraint with a parallel (or anti-parallel) alignment of the relative eccentricity and inclination vectors. This is equivalent to imposing that when the spacecraft crosses the target orbital plane, the radial distance is larger than $\min(a\delta e, a\delta i)$ even in the case of a vanishing along-track separation (D'Amico and Montenbruck, 2006). The only constraint imposed on thrusting angles is to have a null acceleration in radial direction.

The simulation is stopped when all state components reach the target with a tolerance of five meters on their value multiplied by the reference semi-major axis. The resulting trajectory in the LVLH reference frame is shown in Fig. 12, the computed control profile is shown in Fig. 13. The spacecraft completes the transfer with the desired accuracy in less than two orbit periods and, due to the absence of changes in out-of-plane ROE, tangential thrust is sufficient to complete the transfer. The required ΔV amounts to 0.1281 m/s. From the control profile plot, it is possible to notice the saturation of the control effort in the first phases of the transfer. This saturation can be alleviated by reducing the weights of tracking error terms in the MPC cost function, allowing the transfer to be completed in more time in order to improve fuel efficiency. For what concerns attitude control, the spacecraft has enough time to perform all the slewing maneuvers prescribed by the MPC.

5.3. Position swap

To test the effectiveness and efficiency of the collision avoidance algorithm, a setting is created in which two satellites in tandem formation must invert their position while maintaining a minimum inter-satellite distance of 300 meters. The starting and target relative states of the two units with respect to the virtual point placed in the centroid of the formation are listed in form of ROE in Table 11. Also for this simulation radial thrust is set to zero and no further constraint on thrusting angles is added.

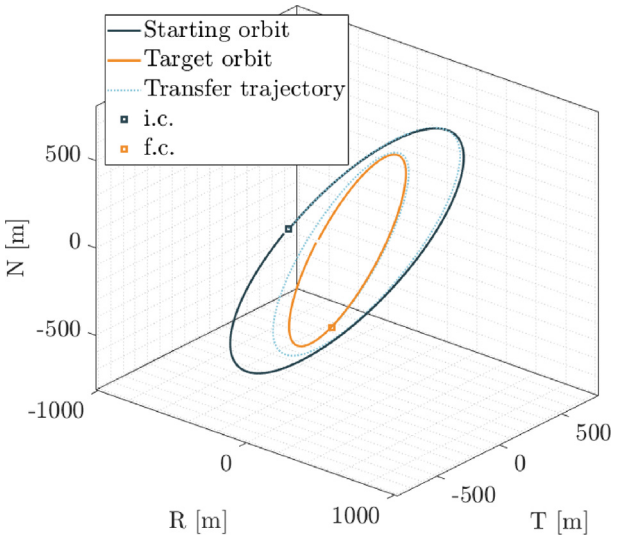

Fig. 12. Transfer trajectory in the LVLH frame for the relative eccentricity change.

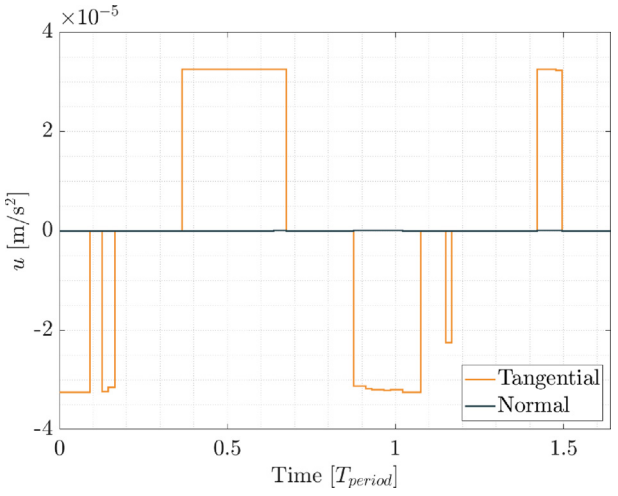

Fig. 13. Control accelerations in the LVLH frame for the relative eccentricity change.

The resulting trajectories in the LVLH frame are shown in Figs. 14 and 15, together with a solution of the same reconfiguration obtained without including the collision avoidance constraint. From the figures, it can be seen how the satellites take a longer path to reach the target in order to keep a minimum relative distance from one to another. This is even more evident in Fig. 16, in which the inter-satellite distance between the two units is represented in its time evolution. With respect to the simulation without collision avoidance, when the constraint is included the transfer takes a longer time and higher ΔV to be concluded, but the safety threshold is always respected. It is also interesting to notice from the figure the prediction ability of the MPC, which is able to deviate the trajectory before reaching the distance threshold.

Table 11
Starting and target relative states for the position swap.

	Spacecraft A	Spacecraft B
i. c.	[0, −200, 0, 0, 0, 0] m	[0, 200, 0, 0, 0, 0] m
f. c.	[0, 200, 0, 0, 0, 0] m	[0, -200, 0, 0, 0, 0] m

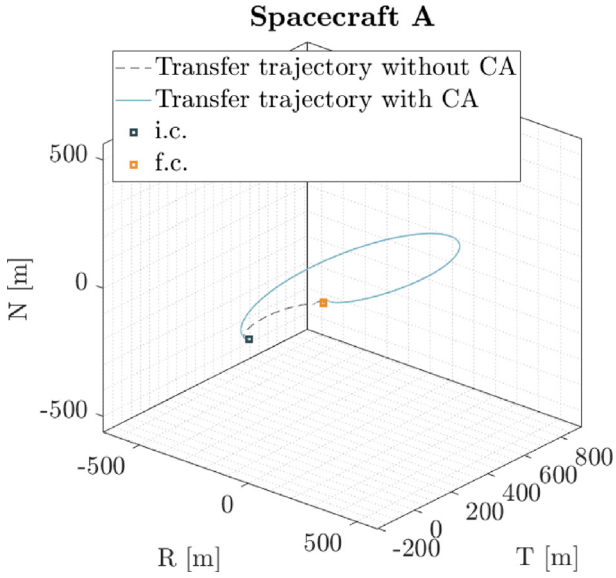

Fig. 14. Transfer trajectory in LVLH frame of Satellite A for the position swap.

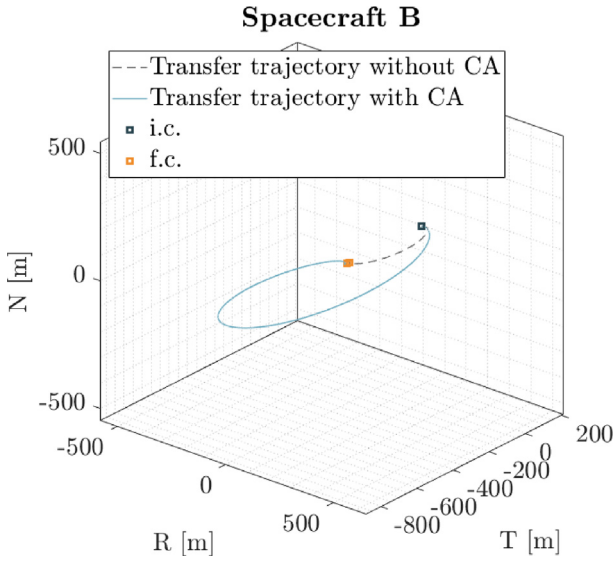

Fig. 15. Transfer trajectory in LVLH frame of Satellite B for the position swap.

5.4. Tetrahedron formation acquisition and maintenance

In previous sections, the MPC is tested in specific scenarios created to isolate some particular response. In the next simulation, a more complex maneuver is simulated, in which four satellites need to acquire and maintain a

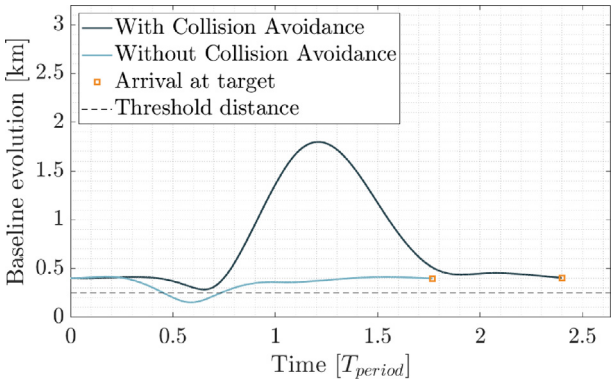

Fig. 16. Inter-satellite distance evolution between the two satellites during the position swap.

Table 12
Starting and target relative states for tetrahedron formation acquisition and maintenance.

	Sat A	Sat B	Sat C	Sat D
$a\delta a$ [m]	$0 \rightarrow 0$	$0 \rightarrow 0$	$0 \rightarrow 0$	$0 \rightarrow 0$
$a\delta\lambda$ [m]	$750 \rightarrow 400$	$250 \rightarrow 100$	$-250 \rightarrow -100$	$-750 \rightarrow -400$
$a\delta e_x$ [m]	$0 \rightarrow 0$	$0 \rightarrow 177$	$0 \rightarrow -177$	$0 \rightarrow 0$
$a\delta e_y$ [m]	$0 \rightarrow 0$	$0 \rightarrow 177$	$0 \rightarrow 177$	$0 \rightarrow 0$
$a\delta i_x$ [m]	$0 \rightarrow 0$	$0 \rightarrow 354$	$0 \rightarrow -354$	$0 \rightarrow 0$
$a\delta i_y$ [m]	$0 \rightarrow 0$	$0 \rightarrow 354$	$0 \rightarrow 354$	$0 \rightarrow 0$

tetrahedron formation geometry starting from an along-track in-line arrangement. Spacecraft flying in tetrahedron formations are excellent instrument platforms for electromagnetic and plasma studies, as a minimum of four units establishing a volume is required to study a planetary magnetic field (Guzman, 2003). To obtain the desired formation shape, the target relative states in ROE formulation have been identified and reported in Table 12, with the ones of the starting string-of-pearls disposition. Satellites A and D remain in line but reduce their relative distance, whereas spacecraft B and C transfer to two bounded orbits slightly separated along-track and with a shifted phase angle of 90°, in order to create a volume.

The phase difference is created by assigning an opposite value of relative eccentricity and relative inclination along the x direction, but equal in the module. This is done to split equally the control needed to counteract the effect of J2 introduced in presence of a δi_x component. Again, the only constraint imposed on thrusting angles is to have a null radial thrust. The evolution in time of the error between the ROE states of the formation and their target value is shown in Fig. 17, the desired relative positions of all satellites are acquired with a ROE accuracy of five meters in slightly less than ten orbital periods. Concerning collision avoidance, no minimum distance is enforced between the satellites, which never cross a minimum baseline between each other of about 50 meters. Naturally, satellites B and C require a higher control effort with respect to the other two formation components, as they need to acquire both relative eccentricity and relative inclination vectors. The resulting ΔV for the four satellites during the tetrahedron acquisition phase are reported in Table 13.

The value for spacecraft B and C can be decreased lowering the gains relative to target tracking, but increasing the transfer time. Values for satellites A and D contain the amount of station keeping that is performed while "waiting" the other two components to complete the transfer. Once the satellites are in the desired position, it is necessary

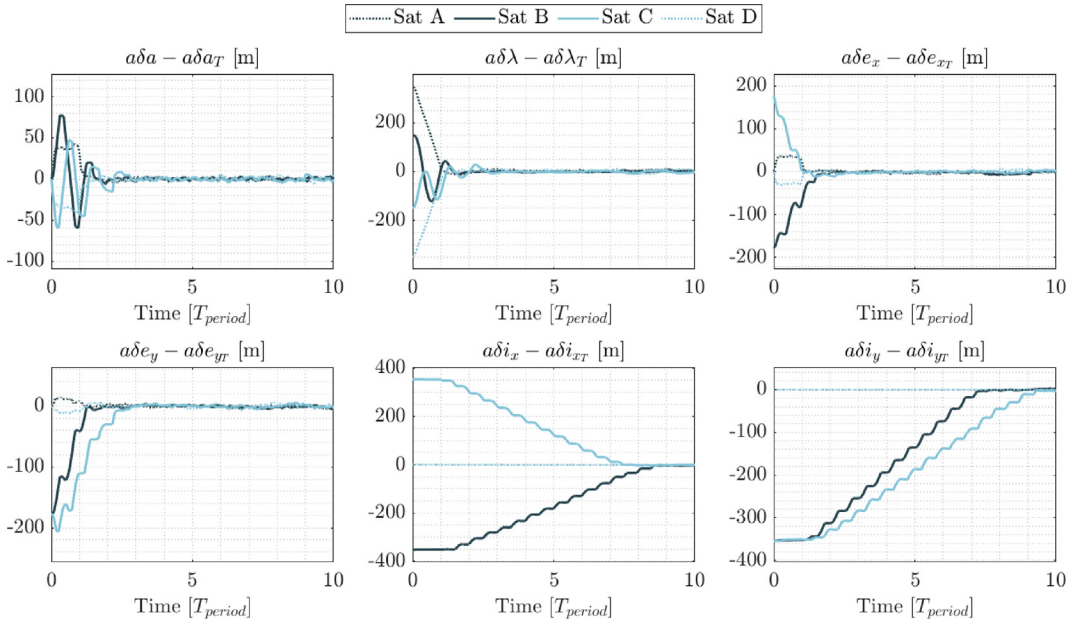

Fig. 17. Evolution in time of the difference between ROE state components and their target value for the four satellites during tetrahedron formation acquisition.

Table 13
Required ΔV for the four satellites to acquire tetrahedron formation geometry.

	ΔV transfer
Sat A	0.1052 m/s
Sat B	0.8643 m/s
Sat C	0.9159 m/s
Sat D	0.1047 m/s

Table 14
Required ΔV to maintain the tetrahedron formation geometry and counteract orbit decay.

	ΔV one day of Station Keeping
Sat A	0.1058 m/s
Sat B	0.1195 m/s
Sat C	0.1213 m/s
Sat D	0.1070 m/s

to maintain the relative states in order to meet the volume-keeping and geometry repetition requirements. To verify the accuracy and efficiency of formation keeping, a simulation of one day is conducted with the spacecraft maintaining not only their respective relative state but also their absolute orbit shape, altitude, in particular, being controlled with respect to a non-decaying orbiting slot. During station keeping, constraints on thrusting angles can be added to prescribe a maximum thrust cone, limiting slew maneuvers during observation. In this case, the in-plane angle is fixed at a value of 0° and the off-plane angle has a maximum variation of 45° around zero. The resulting ΔV for one day of operations is reported in Table 14. The values obtained for satellites A and B are consistent with the ones found in the validation. As expected, units B and C need a slightly higher control effort to counteract the effect of J2 induced by a δi_x component, but this is equally split among the two agents.

In Fig. 18 is represented the evolution in time of the tetrahedral shape of the formation. In particular, the geometry is shown in correspondence of regular values of the argument of latitude of the reference orbit to show its periodic repetition, a usual requirement for tetrahedron formation to guarantee the consistence of measurements. The other two requirements are to keep a constant tetrahedron volume and a constant orbit altitude throughout the observation. The evolution of these two quantities in time is shown in Figs. 19 and 20. The volume is maintained around its nominal value, within a 3σ bound of $1 \cdot 10^{-3}$ km^3. This number, corresponding to about 6% of the reference, is the statistical value under which the variation from the nominal volume is kept for 99.73% of the time. For what concerns drag compensation, it can be observed that

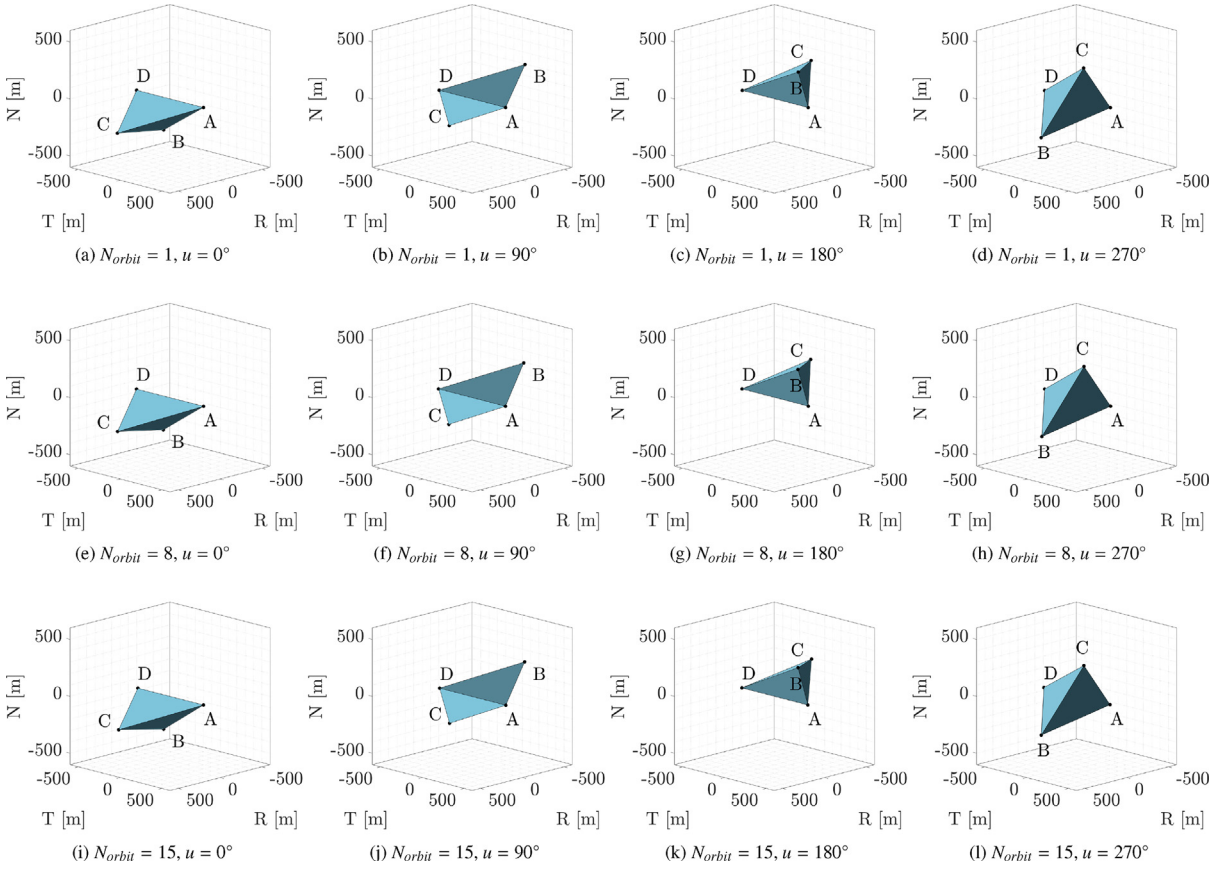

Fig. 18. Evolution in time of the tetrahedron shape during one day of observation. The formation geometry is represented at regular values of the argument of latitude of the reference orbit to show its repetition.

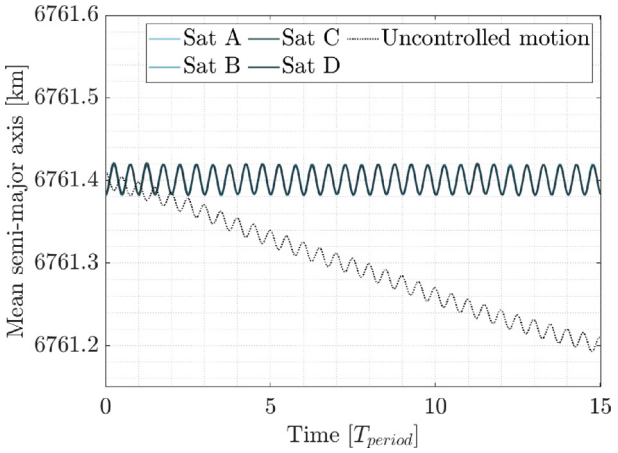

Fig. 19. Mean semi-major axis evolution in time for one day of station keeping.

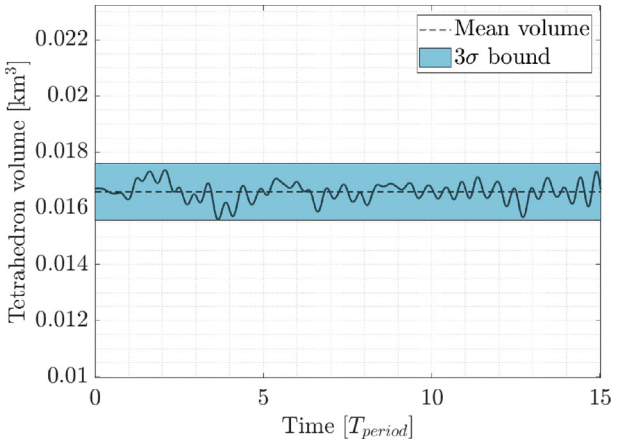

Fig. 20. Tetrahedron volume in time for one day of station keeping.

Table 15
Orbital elements of the HEO orbit.

a [km]	e [-]	i [°]	Ω [°]	ω [°]	M_0 [°]
17445	0.6	63.4	120	270	0

Table 16
Starting and target relative states for the close-up maneuver in HEO.

	$a\delta\boldsymbol{\alpha}$ [m]
i. c.	[0, 0, 0, 500, 0, 500]
f. c.	[0, 0, 0, 200, 0, 200]

the mean semi-major axis is kept constant during the day of observation, whereas an uncontrolled formation would have decayed by a small amount.

Table 17
MPC parameters used for the HEO simulation.

Parameter	Value
Prediction Horizon	11600 s
Sampling time, T_s	200 s
Control Horizon	4 $\cdot T_s$

5.5. Close-up manoeuvre in highly eccentric orbit

The choice of using Relative Orbital Elements instead of the traditional Hills-Clohessy-Wiltshire equations allows to extend the validity of the model to noncircular orbits. To check the accuracy of the algorithm in this environment, a close-up maneuver in High Elliptical Orbit (HEO) is simulated. For this particular case, a Molniya-inspired orbital shape is selected, whose initial keplerian parameters are reported in Table 15. The starting and target relative states are listed in Table 16.

Due to the change of reference orbit with respect to the previous cases, the parameters of the Model Predictive Controller are tuned accordingly. The prediction horizon corresponds to half an orbital period, the sampling time is increased to reduce the computational time of the optimization, and the control horizon is adjusted to find a good trade-off between control accuracy and update frequency. The new values are listed in Table 17.

Even in this application, the MPC shows good accuracy, although slightly lower. Indeed, the simulation is stopped when all ROE reach their target value with a tolerance of ten meters on their value multiplied by the reference semi-major axis. The resulting close-up maneuver is completed with the desired precision in about four orbital periods, the trajectory is shown in Fig. 21. The resulting ΔV needed to perform the transfer amounts to 0.1298 m/s.

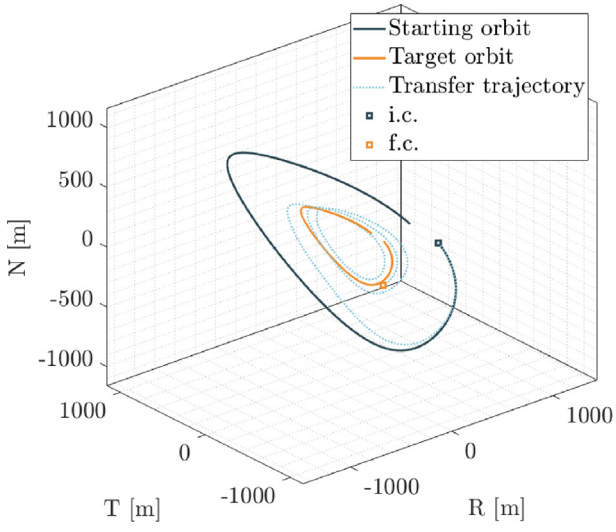

Fig. 21. HEO close-up trajectory in the LVLH frame.

6. Conclusions

To conclude, in this paper a novel on-board Model Predictive Controller for optimal formation acquisition and maintenance in high-drag environment is proposed. The main advanced contributions to the state of the art are:

- The use of a convexified linear dynamics in Relative Orbital Elements in a MPC, instead of the classical cartesian representation in the LVLH reference frame. The formulation is augmented to control the spacecraft both relatively and absolutely in a high-drag environment with respect to a non-decaying orbiting point. For this scope, the derivation of a dedicated plant matrix is proposed.
- The introduction of constraints in the convexified formulation which resemble the limitations of mounting a single low-thrust engine on board, in order to obtain a feasible control profile for an average micro-satellite.

The developed algorithm demonstrated good flexibility in various simulations of formation acquisition, reconfiguration, and maintenance for different relative and absolute orbit shapes. For what concerns fuel efficiency, in the simpler manoeuvres isolating in-plane or out-of-plane control, the MPC was able to provide a close to optimal result. On the other hand, when these two components are mixed, or in particularly challenging scenarios, fuel-optimality can be improved. This is most evident for satellites B and C in the tetrahedron acquisition scenario, in which they needed to acquire both relative eccentricity and relative inclination components and the trajectories of the four spacecrafts were optimized at the same time by the MPC. On the other hand, the ΔV that was provided for drag compensation and station keeping was consistent for all simulated scenarios with the optimal results provided in the validation. The accuracy that was provided by the MPC was good in all simulations, in which the spacecrafts were able to acquire the desired states and maintain them with an accuracy in the order of meters. In addition, the collision avoidance constraint demonstrated to be effective in computing safe trajectories which respected the threshold distance in situations where its inclusion was necessary. Finally, limits on thrust module and angles were always satisfied in all applications and the slew rate constraint proved to avoid immediate 180° rotations, providing some time to reorientate the engine.

Declaration of Competing Interest

The authors declare that they have no known competing financial interests or personal relationships that could have appeared to influence the work reported in this paper.

References

Acikmese, B., Scharf, D., Hadaegh, F. et al., 2012. A convex guidance algorithm for formation reconfiguration. In: AIAA Guidance, Navigation, and Control Conference and Exhibit. https://doi.org/10.2514/6.2006-6070. URL: https://arc.aiaa.org/doi/abs/10.2514/6.2006-6070. arXiv:https://arc.aiaa.org/doi/pdf/10.2514/6.2006-6070.

Agrawal, A., Verschueren, R., Diamond, S., et al., 2018. A rewriting system for convex optimization problems. J. Control Decis. 5 (1), 42–60. https://doi.org/10.1080/23307706.2017.1397554.

Bai, X., He, Y., Xu, M., 2021. Low-thrust reconfiguration strategy and optimization for formation flying using jordan normal form. IEEE Trans. Aerosp. Electron. Syst. 57 (5), 3279–3295. https://doi.org/10.1109/TAES.2021.3074204.

Bai, X., Huang, M., Xu, M., et al., 2023. Reconfiguration optimization of relative motion between elliptical orbits using lyapunov-floquet transformation. IEEE Trans. Aerosp. Electron. Syst. 59 (2), 923–936. https://doi.org/10.1109/TAES.2022.3193089.

Battin, R., 1999. An Introduction to the Mathematics and Methods of Astrodynamics. AIAA education series. American Institute of Aeronautics and Astronautics, New York.

Bowman, B., Marcos, F., Huang, C., et al., 2008. A new empirical thermospheric density model jb2008 using new solar and geomagnetic indices. In: AIAA/AAS Astrodynamics Specialist Conference and Exhibit. https://doi.org/10.2514/6.2008-6438.

Catanoso, D., Kempf, F., Schilling, K. et al., 2019. Networked model predictive control for satellite formation flying. In: 10th International Workshop of Satellites Constellations and Formation Flying.

Chernick, M., D'Amico, S., 2018. New closed-form solutions for optimal impulsive control of spacecraft relative motion. J. Guidance Control Dyn. 41 (2), 301–319. https://doi.org/10.2514/1.G002848, arXiv:https://doi.org/10.2514/1.G002848.

Clohessy, W.H., Wiltshire, R.S., 1960. Terminal guidance system for satellite rendezvous. J. Aerospace Sci. 27 (9), 653–658. https://doi.org/10.2514/8.8704.

D'Amico, S., 2010. Autonomous formation flying in low earth orbit. Ph. D. thesis TU Delft.

D'Amico, S., Montenbruck, O., 2006. Proximity operations of formation-flying spacecraft using an eccentricity/inclination vector separation. J. Guidance Control Dyn. 29 (3), 554–563. https://doi.org/10.2514/1.15114, arXiv:https://doi.org/10.2514/1.15114.

Diamond, S., Boyd, S., 2016. Cvxpy: A python-embedded modeling language for convex optimization. J. Machine Learn. Res. 17 (1), 2909–2913.

Gaias, G., Ardaens, J., Montenbruck, O., 2015. Model of J2 perturbed satellite relative motion with time-varying differential drag. Celestial Mech. Dyn. Astron. 123 (4), 411–433. https://doi.org/10.1007/s10569-015-9643-2.

Grant, M., Boyd, S., 2008. Graph implementations for nonsmooth convex programs. In: Blondel, V., Boyd, S., Kimura, H. (Eds.), Recent Advances in Learning and Control Lecture Notes in Control and Information Sciences. Springer-Verlag Limited, pp. 95–110.

Grant, M., Boyd, S., 2014. CVX: Matlab software for disciplined convex programming, version 2.1. http://cvxr.com/cvx.

Guffanti, T., D'Amico, S., Lavagna, M., 2017. Long-term analytical propagation of satellite relative motion in perturbed orbits. In: 27th AAS/AIAA Space Flight Mechanics Meeting.

Guzman, J.J., 2003. Tetrahedron Formation Control. Technical Report a. i. solutions, Inc.

Koenig, A.W., Guffanti, T., D'Amico, S., 2017. New state transition matrices for spacecraft relative motion in perturbed orbits. J. Guidance Control Dyn. 40 (7), 1749–1768. https://doi.org/10.2514/1.G002409.

McInnes, C.R., 1995. Autonomous ring formation for a planar constellation of satellites. J. Guidance Control Dyn. 18 (5), 1215–1217. https://doi.org/10.2514/3.21531, arXiv:https://doi.org/10.2514/3.21531.

Morgan, D., Chung, S.-J., Blackmore, L., et al., 2012. Swarm-keeping strategies for spacecraft under j2 and atmospheric drag perturbations. J. Guidance Control Dyn. 35 (5), 1492–1506. https://doi.org/10.2514/1.55705.

Morgan, D., Chung, S.-J., Hadaegh, F.Y., 2014. Model predictive control of swarms of spacecraft using sequential convex programming. J.

Guidance Control Dyn. 37 (6), 1725–1740. https://doi.org/10.2514/1.G000218, arXiv:https://doi.org/10.2514/1.G000218.

Palmerini, G.B., 1999. Guidance strategies for satellite formations. In: Advances in the Astonautical Sciences, vol. 103, pp. 135–145.

Sarno, S., Guo, J., D'Errico, M., et al., 2020. A guidance approach to satellite formation reconfiguration based on convex optimization and genetic algorithms. Adv. Space Res. 65 (8), 2003–2017. https://doi.org/10.1016/j.asr.2020.01.033, URL: https://www.sciencedirect.com/science/article/pii/S0273117720300673.

Scala, F., Gaias, G., Colombo, C., et al., 2021. Design of optimal low-thrust manoeuvres for remote sensing multi-satellite formation flying in low earth orbit. Adv. Space Res. 68 (11), 4359–4378. https://doi.org/10.1016/j.asr.2021.09.030, URL: https://www.sciencedirect.com/science/article/pii/S0273117721007456.

Silvestrini, S., Lavagna, M., 2021. Neural-aided gnc reconfiguration algorithm for distributed space system: development and pil test. Adv. Space Res. 67 (5), 1490–1505. https://doi.org/10.1016/j.asr.2020.12.014, URL: https://www.sciencedirect.com/science/article/pii/S027311772030870X.

Silvestrini, S., Pesce, V., Lavagna, M., 2019. Distributed Autonomous Guidance, Navigation and Control loop for Formation Flying Spacecraft Reconfiguration. In: EUROGNC19 – 5th CEAS Conference on Guidance, Navigation & Control.

Steindorf, L., D'Amico, S., Scharnagl, J. et al., 2017. Constrained Low-thrust satellite formation-flying using relative orbit elements. In: 27th AAS/AIAA Space Flight Mechanics Meeting.

Sturm, J.F., 1999. Using sedumi 1.02, a matlab toolbox for optimization over symmetric cones. Optim. Methods Softw. 11 (1–4), 625–653. https://doi.org/10.1080/10556789908805766.

Toh, K.C., Todd, M.J., Tütüncü, R.H., 1999. Sdpt3 — a matlab software package for semidefinite programming, version 1.3. Optim. Methods Softw. 11 (1–4), 545–581. https://doi.org/10.1080/10556789908805762.

Wu, B., Wang, D., Poh, E.K., et al., 2009. Nonlinear optimization of low-thrust trajectory for satellite formation: Legendre pseudospectral approach. J. Guidance Control Dyn. 32 (4), 1371–1381. https://doi.org/10.2514/1.37675, arXiv:https://doi.org/10.2514/1.37675.

Zheng, Y., Xu, M., Luo, T., et al., 2019. Application of floquet theory to formation flying in elliptic orbits via a hamiltonian structure-preserving control. Aerosp. Sci. Technol. 95, 105508. https://doi.org/10.1016/j.ast.2019.105508, URL: https://www.sciencedirect.com/science/article/pii/S1270963818327378.